INTERNATIONAL JOURNAL FOR NUMERICAL METHODS IN FLUIDS
Int. J. Numer. Meth. Fluids 2008; **56**:607–627
Published online 27 June 2007 in Wiley InterScience (www.interscience.wiley.com). DOI: 10.1002/fld.1542

A three-dimensional non-hydrostatic vertical boundary fitted model for free-surface flows

Peyman Badiei[‡], Masoud M. Namin[‡] and Afshin Ahmadi[*, †]

School of Civil Engineering, University College of Engineering, University of Tehran, P.O. Box 11365-4563, Tehran, Iran

SUMMARY

A non-hydrostatic finite volume model is presented to simulate three-dimensional (3D) free-surface flows on a vertical boundary fitted grid system. The algorithm, which is an extension to the previous two dimensional vertical (2DV) model proposed by Ahmadi *et al*. (*Int. J. Numer. Meth. Fluids* 2007; **54**(9):1055–1074), solves the complete 3D Navier–Stokes equations in two major steps based on projection method. First, by excluding the pressure terms in momentum equations, a set of advection–diffusion equations are obtained. In the second step, the continuity and the momentum equations with the remaining pressure terms are solved which yields a block tri-diagonal system of equations with pressure as the unknown. In this step, the 3D system is decomposed into a series of 2DV plane sub-systems which are solved individually by a direct matrix solver. Iteration is required to ensure convergence of global 3D system. To minimize the number of vertical layers and subsequently the computational cost, a new top-layer pressure treatment is proposed which enables the model to simulate a range of surface waves using only 2–5 vertical layers.

Received 27 December 2006; Revised 18 April 2007; Accepted 19 April 2007

KEY WORDS: projection method; finite volume method; non-hydrostatic models; free-surface flow; vertical boundary fitted; top-layer treatment

1. INTRODUCTION

Long waves such as tides with periods in the order of hours can be successfully simulated assuming a hydrostatic pressure distribution in depth. This assumption is no more valid when short waves with periods in the order of few seconds are to be simulated and deploying a dynamic pressure distribution is necessary. Such non-hydrostatic models have been developed recently by Chorin [1],

*Correspondence to: Afshin Ahmadi, School of Civil Engineering, University College of Engineering, University of Tehran, P.O. Box 11365-4563, Tehran, Iran.
†E-mail: afahmadi@ut.ac.ir, afsh_ahmadi@yahoo.com
‡Assistant Professor.

Contract/grant sponsor: Water Resources Management Co.; contract/grant number: RIV1-83084
Contract/grant sponsor: University of Tehran

Li and Fleming [2] and Lin and Li [3] using explicit projection method. Casulli [4], Kocyigit *et al.* [5] and Chen [6] deployed semi-implicit fractional method. A fully non-hydrostatic implicit algorithm was suggested by Namin *et al.* [7] and Yuan and Wu [8, 9] by solving the governing equations simultaneously and in one stage, in terms of horizontal velocity as unknown. Ahmadi *et al.* [10] developed an implicit finite volume two-dimensional vertical (2DV) model on a sigma coordinate like mesh to simulate free-surface flows. The algorithm, based on projection method, solved the complete 2DV Navier–Stokes equation (NSE) with pressure as unknown.

Although depth-integrated models based on Mild-slope and Boussinesq equations have been successfully applied to simulate short wave propagation, they are unable to predict the variation of flow structure within depth. In order to obtain a better understanding of these variations, 2DV and three-dimensional (3D) models should be applied.

The moving free-surface forms the upper boundary of the computational domain which is itself a part of the solution. One class of free-surface flow models simulates the details of this boundary. Schemes such as marker and cell [11], volume of fluid [12], arbitrary Lagrangian–Eulerian [13] and level-set method [14] are among the methods of this class. All of these methods are associated with relatively large computational cost. On the other hand by applying mass conservation to the water column and kinematic free-surface boundary condition, the free-surface elevation is defined as a single valued function of horizontal location [2–10]. This method can be applied to a wide variety of problems with comparatively large computational domains, using less CPU time.

In some non-hydrostatic models, a hydrostatic pressure distribution is assumed at the top layer and a large number of vertical layers are necessary to simulate non-hydrostatic free-surface flows [2, 7]. Yuan and Wu [8] planned an integral technique in sigma coordinate framework to remove the top-layer hydrostatic pressure assumption. Their results demonstrate that by applying non-hydrostatic pressure distribution to the top layer, phase errors are noticeably reduced in the simulation of dispersive waves. Stelling and Zijlema [15] presented an approximation of vertical gradient of the non-hydrostatic pressure based on the Keller-box or Preissmann scheme. As a result of the fact that the scheme is edge based with respect to pressure in vertical direction, the zero pressure boundary condition at free surface can be approximated very accurately. Their results show that this procedure allows very small number of layers (in the order of 1–3) for the simulation of relatively short waves. Recognizing the popularity of staggered grid system, following Stelling and Zijlema [15], Yuan and Wu [9, 16] switched from sigma to Cartesian coordinate system and proposed another integral method, different from the Keller-box scheme, to obtain non-hydrostatic pressure condition at the free-surface cell. Using a small number of vertical layers, they also showed the model can accurately simulate very steep waves (steepness up to 0.31). As well they found that the number of vertical layers depends on a dimensionless number—the product of wave number and water depth [16]. Subsequently Choi and Wu [17] changed the numerical algorithm to projection method in which, the size of resulting matrix, is a quarter smaller than pervious Yuan and Wu [9, 16] work. Their satisfactory results demonstrated the capability of modelling a range of waves with small number of vertical layers.

For the numerical solution of 3D system of NSE, various methods have been proposed. Iterative conjugate gradient technique was applied by Kocyigit [5] and generalized minimal residual method with symmetric Gauss–Seidel preconditioning was deployed by Lee *et al.* [18]. Yuan and Wu [9] decomposed the 3D system into a series of 2DV problems, for each of which a block tri-diagonal system of equations with unknown horizontal velocity was solved. An iteration procedure is then applied to ensure the overall convergence. Choi and Wu [17] deployed a bi-conjugate gradient method with a pre-conditioning procedure to solve the resulting matrix system.

DOI: 10.1002/fld

In this paper, a vertical boundary fitted finite volume model for free-surface flows is presented which solves the complete form of 3D NSE. The algorithm is based on time splitting method which solves the equations in two major steps. First the pressure term in the momentum equations is excluded and the resultant 3D advection–diffusion equations are solved. In the second step, the continuity and the momentum equation with only the pressure terms are solved to give a system of equations in terms of pressure. In this step, the 3D system of equations is decomposed into 2DV sub-systems. Each sub-system can be solved by a direct matrix solver. An iteration procedure is used to guarantee the convergence of 3D system at the end. With this algorithm, the water elevation can be obtained along with the velocity and pressure fields as a part of the solution. To minimize the computational cost, a new top-layer pressure treatment is proposed. This method enables the model to simulate wave motion with only a few vertical layers accurately. Vertical boundary fitted grid system has been chosen as the computational mesh, which enables the model to simulate free-surface flows over irregular geometries. Section 2 presents the governing equations together with boundary conditions. The numerical method is explained in Section 3. In Section 4, the model is validated by four tests using very small number of vertical layers, including a linear 3D standing short wave in deep water, linear progressive wave, solitary wave propagation over variable water depths and 3D nonlinear wave propagation over a submerged elliptic shoal. Numerical results are validated against analytical solutions or experimental data.

2. MATHEMATICAL FORMULATION

The governing equations used to describe the 3D, incompressible flows are based on the conservation of mass and momentum. Dividing pressure p into two parts, namely the 'hydrostatic pressure' and 'excess pressure' P^*, ($P = -\rho g z + \rho P^*$), the following equations are obtained:

$$\frac{\partial u}{\partial x} + \frac{\partial v}{\partial y} + \frac{\partial w}{\partial z} = 0 \tag{1}$$

$$\frac{\partial u}{\partial t} + \frac{\partial u^2}{\partial x} + \frac{\partial uv}{\partial y} + \frac{\partial uw}{\partial z} + \frac{\partial P^*}{\partial x} = \frac{\partial}{\partial x}\left(\nu_t \frac{\partial u}{\partial x}\right) + \frac{\partial}{\partial y}\left(\nu_t \frac{\partial u}{\partial y}\right) + \frac{\partial}{\partial z}\left(\nu_t \frac{\partial u}{\partial z}\right) \tag{2}$$

$$\frac{\partial v}{\partial t} + \frac{\partial vu}{\partial x} + \frac{\partial v^2}{\partial y} + \frac{\partial vw}{\partial z} + \frac{\partial P^*}{\partial y} = \frac{\partial}{\partial x}\left(\nu_t \frac{\partial v}{\partial x}\right) + \frac{\partial}{\partial y}\left(\nu_t \frac{\partial v}{\partial y}\right) + \frac{\partial}{\partial z}\left(\nu_t \frac{\partial v}{\partial z}\right) \tag{3}$$

$$\frac{\partial w}{\partial t} + \frac{\partial wu}{\partial x} + \frac{\partial wv}{\partial y} + \frac{\partial w^2}{\partial z} + \frac{\partial P^*}{\partial z} = \frac{\partial}{\partial x}\left(\nu_t \frac{\partial w}{\partial x}\right) + \frac{\partial}{\partial y}\left(\nu_t \frac{\partial w}{\partial y}\right) + \frac{\partial}{\partial z}\left(\nu_t \frac{\partial w}{\partial z}\right) \tag{4}$$

where t is the time; u,v and w are components of velocity in the x,y and z directions, respectively; ρ is the density of water; g is the gravitational acceleration; and ν_t is the eddy viscosity coefficient.

2.1. Boundary conditions

The kinematic boundary condition at the impermeable bottom is

$$u\frac{\partial h}{\partial x} + v\frac{\partial h}{\partial y} + w = 0 \tag{5}$$

DOI: 10.1002/fld

where h is the still water depth. At impermeable bottom and wall boundaries zero normal velocity is applied. For viscous flows no-slip boundary condition is considered. In non-viscous flows, tangential velocity gradient at wall boundaries is set to zero. Similarly, the kinematic boundary condition at the moving free-surface is

$$\frac{\partial \xi}{\partial t} + u\frac{\partial \xi}{\partial x} + v\frac{\partial \xi}{\partial y} = w \tag{6}$$

where ξ is the surface elevation. Using kinematic boundary conditions (5) and (6) in the integrated form of the continuity equation (1) over the water column, the free-surface equation is obtained:

$$\frac{\partial \xi}{\partial t} + \frac{\partial}{\partial x}\int_{-h}^{\xi} u \, \mathrm{d}z + \frac{\partial}{\partial y}\int_{-h}^{\xi} v \, \mathrm{d}z = 0 \tag{7}$$

Atmospheric pressure is assumed at free-surface elevation. Measured laboratory or theoretical velocity distribution in the vertical direction are adopted as inflow boundary conditions. Sponge layer technique [9, 11] is implemented at outflow boundaries to eliminate wave reflection.

3. NUMERICAL METHOD

A finite volume approximation is used to discretize the governing equations and boundary conditions. A vertical boundary fitted (sigma coordinate like) staggered grid system with a set of N_1, N_2 and N_3 cells, respectively, in longitudinal and vertical direction is employed. In this system, the number of vertical layers across the whole domain is constant and the curvature applies only in the horizontal directions. The mesh projection on horizontal plane forms a rectilinear grid system. Figure 1 shows the physical domain and the definition of main variables. The pressure points have been considered to be placed on the cell centre denoted by $(2i, 2j, 2k)$. The u, v and w velocities are located at the faces i.e. $(2i \pm 1, 2j, 2k)$, $(2i, 2j \pm 1, 2k)$ and $(2i, 2j, 2k \pm 1)$, respectively.

3.1. Numerical techniques

A fractional step algorithm is deployed to solve the governing equations in two major steps. In the first step, the momentum equations excluding the pressure gradient terms are solved. This step is subdivided into two stages, namely 'advection' and 'diffusion'. In the second step, the continuity equation, together with the momentum equations without advection and diffusion terms are solved. In this step, following Yuan and Wu [9] the whole 3D domain is decomposed into a series of 2DV sub-domains. Every 2DV sub-domain yields a block tri-diagonal matrix system with the unknown pressure, which can be solved by a direct matrix solver. The calculated values are considered as temporary and iteration is carried out to ensure the convergence of the solution. It should be noted that the derivatives in the normal direction to each sub-domain plain are obtained from previous iteration or time step.

3.1.1. Step I. In the first step, momentum equations (2)–(4) excluding the pressure gradient terms are solved. This step is subdivided into two stages, namely 'advection' and 'diffusion'. In stage 1,

DOI: 10.1002/fld

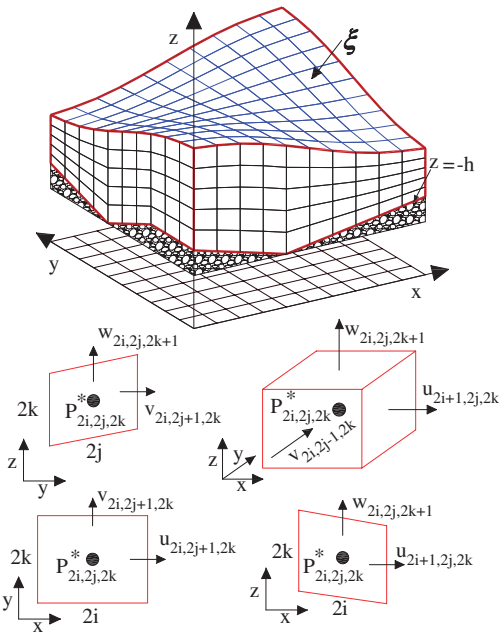

Figure 1. Presentation of physical domain, staggered grids and the positions of the variables.

velocities are advected using the known velocity field at the previous time step n, to obtain the new intermediate velocity field u^*, v^* and w^*, where

$$\frac{u^* - u^n}{\Delta t} = -\left[\frac{\partial(u^2)}{\partial x} + \frac{\partial(uv)}{\partial y} + \frac{\partial(uw)}{\partial z}\right]^n \tag{8}$$

$$\frac{v^* - v^n}{\Delta t} = -\left[\frac{\partial(vu)}{\partial x} + \frac{\partial(v^2)}{\partial y} + \frac{\partial(vw)}{\partial z}\right]^n \tag{9}$$

$$\frac{w^* - w^n}{\Delta t} = -\left[\frac{\partial(wu)}{\partial x} + \frac{\partial(wv)}{\partial y} + \frac{\partial(w^2)}{\partial z}\right]^n \tag{10}$$

An upwind explicit numerical scheme is used to solve advection stage. In the next stage, the diffusion terms are solved to find second intermediate velocities u^{**}, v^{**} and w^{**}, wherein

$$\frac{u^{**} - u^*}{\Delta t} = \frac{\partial}{\partial x}\left(v_t \frac{\partial u^{**}}{\partial x}\right) + \frac{\partial}{\partial y}\left(v_t \frac{\partial u^{**}}{\partial y}\right) + \frac{\partial}{\partial z}\left(v_t \frac{\partial u^{**}}{\partial z}\right) \tag{11}$$

$$\frac{v^{**} - v^*}{\Delta t} = \frac{\partial}{\partial x}\left(v_t \frac{\partial v^{**}}{\partial x}\right) + \frac{\partial}{\partial y}\left(v_t \frac{\partial v^{**}}{\partial y}\right) + \frac{\partial}{\partial z}\left(v_t \frac{\partial v^{**}}{\partial z}\right) \tag{12}$$

$$\frac{w^{**} - w^*}{\Delta t} = \frac{\partial}{\partial x}\left(v_t \frac{\partial w^{**}}{\partial x}\right) + \frac{\partial}{\partial y}\left(v_t \frac{\partial w^{**}}{\partial y}\right) + \frac{\partial}{\partial z}\left(v_t \frac{\partial w^{**}}{\partial z}\right) \tag{13}$$

Crank–Nicholson scheme has been applied for solving Equations (11)–(13).

DOI: 10.1002/fld

3.1.2. Step II. In the second step, continuity equation (1) together with the momentum equations excluding advection and diffusion terms are solved as follows:

$$\left(\frac{\partial u}{\partial x}\right)^{n+1} + \left(\frac{\partial v}{\partial y}\right)^{n+1} + \left(\frac{\partial w}{\partial z}\right)^{n+1} = 0 \tag{14}$$

$$\frac{u^{n+1} - u^{**}}{\Delta t} + \left(\psi\left(\frac{\partial P^*}{\partial x}\right)^{n+1} + (1-\psi)\left(\frac{\partial P^*}{\partial x}\right)^{n}\right) = 0 \tag{15}$$

$$\frac{v^{n+1} - v^{**}}{\Delta t} + \left(\psi\left(\frac{\partial P^*}{\partial y}\right)^{n+1} + (1-\psi)\left(\frac{\partial P^*}{\partial y}\right)^{n}\right) = 0 \tag{16}$$

$$\frac{w^{n+1} - w^{**}}{\Delta t} + \left(\psi\left(\frac{\partial P^*}{\partial z}\right)^{n+1} + (1-\psi)\left(\frac{\partial P^*}{\partial z}\right)^{n}\right) = 0 \tag{17}$$

3.1.2.1. x-derivative approximation. The x derivative of horizontal velocity (u) at point ($2i, 2j, 2k$) in x–z plane is written as [10]

$$\left(\frac{\partial u}{\partial x}\right)_{2i,2j,2k} \approx \sum_{j1=1}^{2}\sum_{j2=1}^{3} r(xz)_{j1,j2}^{2i,2j,2k} u_{m_{2i}(j1),2j,n_{2k}(j2)} \tag{18}$$

where

$$m_{2i}(1) = 2i - 1, \quad m_{2i}(2) = 2i + 1$$

$$n_{2k}(1) = 2k - 2, \quad n_{2k}(2) = 2k, \quad n_{2k}(3) = 2k + 2$$

$$\mathbf{r}(xz)^{2i,2j,2k} = \begin{bmatrix} \dfrac{s_{2i,2j,2k-1}}{4\Delta z_{2i,2j}} & -\dfrac{\Delta z_{2i-1,2j}}{\mathrm{Ar}} + \dfrac{s_{2i,2j,2k-1}}{4\Delta z_{2i,2j}} - \dfrac{s_{2i,2j,2k+1}}{4\Delta z_{2i,2j}} & -\dfrac{s_{2i,2j,2k+1}}{4\Delta z_{2i,2j}} \\ \dfrac{s_{2i,2j,2k-1}}{4\Delta z_{2i,2j}} & +\dfrac{\Delta z_{2i+1,2j}}{\mathrm{Ar}} + \dfrac{s_{2i,2j,2k-1}}{4\Delta z_{2i,2j}} - \dfrac{s_{2i,2j,2k+1}}{4\Delta z_{2i,2j}} & -\dfrac{s_{2i,2j,2k+1}}{4\Delta z_{2i,2j}} \end{bmatrix}$$

$\mathrm{Ar} = \Delta x \Delta z_{2i,2j}$ is the area of the control volume, $\Delta z_{2i,2j}$ is the space interval in the vertical direction of column ($2i, 2j$), which for an equidistant sigma coordinate case, does not vary with k. $s_{2i,2j,2k-1}$ and $s_{2i,2j,2k+1}$ are the slopes of the longitudinal edges of the control volume in $x-z$ plane, placed at the location of $2i, 2j, 2k-1$ and $2i, 2j, 2k+1$, respectively. The x derivative of pressure on cells centre can be derived from the above procedure by shifting the formulation from $2i$ to $2i+1$.

3.1.2.2. y-derivative approximation. Similarly, the y derivative of the horizontal velocity (v) at point ($2i, 2j, 2k$) in y–z plane is written as follows:

$$\left(\frac{\partial v}{\partial y}\right)_{2i,2j,2k} \approx \sum_{j1=1}^{2}\sum_{j2=1}^{3} r(yz)_{j1,j2}^{2i,2j,2k} v_{2i,m_{2j}(j1),n_{2k}(j2)} \tag{19}$$

DOI: 10.1002/fld

where

$$m_{2j}(1) = 2j - 1, \quad m_{2j}(2) = 2j + 1$$

$$\mathbf{r}(yz)^{2i,2j,2k} = \begin{bmatrix} \dfrac{s_{2i,2j,2k-1}}{4\Delta z_{2i,2j}} & -\dfrac{\Delta z_{2i,2j-1}}{\mathrm{Ar}} + \dfrac{s_{2i,2j,2k-1}}{4\Delta z_{2i,2j}} - \dfrac{s_{2i,2j,2k+1}}{4\Delta z_{2i,2j}} & -\dfrac{s_{2i,2j,2k+1}}{4\Delta z_{2i,2j}} \\ \dfrac{s_{2i,2j,2k-1}}{4\Delta z_{2i,2j}} & +\dfrac{\Delta z_{2i,2j+1}}{\mathrm{Ar}} + \dfrac{s_{2i,2j,2k-1}}{4\Delta z_{2i,2j}} - \dfrac{s_{2i,2j,2k+1}}{4\Delta z_{2i,2j}} & -\dfrac{s_{2i,2j,2k+1}}{4\Delta z_{2i,2j}} \end{bmatrix}$$

Here $\mathrm{Ar} = \Delta y \Delta z_{2i,2j}$ is the area of the control volume, $s_{2i,2j,2k-1}$ and $s_{2i,2j,2k+1}$ are the slopes of the longitudinal edges of the control volume in y–z plane.

3.1.2.3. Solution of 3D equations. Using Equations (15)–(17) and applying the derivative definitions, the horizontal and vertical velocities can be written in the following form:

$$u^{n+1}_{2i-1,2j,2k} = d_{2i-1,2j,2k} - \psi \Delta t \sum_{j1=1}^{2} \sum_{j2=1}^{3} r(xz)^{2i-1,2j,2k}_{j1,j2} P^{*n+1}_{m_{2i-1}(j1),2j,n_{2k}(j2)} \tag{20}$$

$$v^{n+1}_{2i,2j-1,2k} = d_{2i,2j-1,2k} - \psi \Delta t \sum_{j1=1}^{2} \sum_{j2=1}^{3} r(yz)^{2i,2j-1,2k}_{j1,j2} P^{*n+1}_{2i,m_{2j-1}(j1),n_{2k}(j2)} \tag{21}$$

$$w^{n+1}_{2i,2j,2k-1} = d_{2i,2j,2k-1} - \psi \Delta t \left(\frac{P^{*n+1}_{2i,2j,2k} - P^{*n+1}_{2i,2j,2k-2}}{\Delta z_{2i,2j}} \right) \tag{22}$$

where

$$d_{2i-1,2j,2k} = u^{**}_{2i-1,2j,2k} - (1-\psi)\Delta t \sum_{j1=1}^{2} \sum_{j2=1}^{3} r(xz)^{2i-1,2j,2k}_{j1,j2} P^{*n}_{m_{2i-1}(j1),2j,n_{2k}(j2)} \tag{23}$$

$$d_{2i,2j-1,2k} = v^{**}_{2i,2j-1,2k} - (1-\psi)\Delta t \sum_{j1=1}^{2} \sum_{j2=1}^{3} r(yz)^{2i,2j-1,2k}_{j1,j2} P^{*n}_{2i,m_{2j-1}(j1),n_{2k}(j2)} \tag{24}$$

$$d_{2i,2j,2k-1} = w^{**}_{2i,2j,2k-1} - (1-\psi)\Delta t \left(\frac{P^{*n}_{2i,2j,2k} - P^{*n}_{2i,2j,2k-2}}{\Delta z_{2i,2j}} \right) \tag{25}$$

The weighting factor ψ, is taken as 0.5. Equations (20)–(22) define each velocity component in terms of the pressure located upstream and downstream of these velocity components, respectively. By substituting these values into continuity equation (14), the velocities can be eliminated to give an equation in terms of pressure. These equations will be presented in the next sections.

Decomposition into 2DV planes: A domain decomposition method similar to [9] is deployed to solve Equations (14)–(17). The original 3D problem is separated to a series of 2DV sub-problems. Orthogonal to the plane derivatives in these equations, i.e. $(\partial/\partial y)$ in the x–z plane and $(\partial/\partial x)$ in the y–z plane are calculated based on the known values of the previous time step or iteration shown with superscript $n + \alpha$.

DOI: 10.1002/fld

An iteration process is deployed to guarantee the convergence of solution. First, we set $u^{n+\alpha}=u^n$ and $v^{n+\alpha}=v^n$. Secondly, each vertical plane in x–z and y–z are solved to give updated horizontal velocities u^{n+1} and v^{n+1}, respectively. We set again $u^{n+\alpha}=u^{n+1}$ and $v^{n+\alpha}=v^{n+1}$ and solve each vertical planes for second time. This procedure is repeated until $|u^{n+1}-u^{n+\alpha}|<\varepsilon$ and $|v^{n+1}-v^{n+\alpha}|<\varepsilon$, where ε is a criterion for convergence.

Solving of equations in x–z planes: The derivatives of the u and w velocities at the new time level $n+1$ can be expressed by using Equations (20) and (22), respectively, as

$$\left(\frac{\partial u}{\partial x}\right)^{n+1}_{2i,2j,2k} \approx \sum_{j1=1}^{2}\sum_{j2=1}^{3} r(xz)^{2i,2j,2k}_{j1,j2} u^{n+1}_{m_{2i}(j1),2j,n_{2k}(j2)}$$

$$= \sum_{j1=1}^{2}\sum_{j2=1}^{3} r(xz)^{2i,2j,2k}_{j1,j2} d_{m_{2i}(j1),2j,n_{2k}(j2)}$$

$$- \psi\Delta t \sum_{j1=1}^{2}\sum_{j2=1}^{3} r(xz)^{2i,2j,2k}_{j1,j2}$$

$$\times \left(\sum_{j3=1}^{2}\sum_{j4=1}^{3} r(xz)^{m_{2i}(j1),2j,n_{2k}(j2)}_{j3,j4} P^{*n+1}_{m_{m_{2i}(j1)}(j3),n_{n_{2k}(j2)}(j4)}\right) \tag{26}$$

$$\left(\frac{\partial w}{\partial z}\right)^{n+1}_{2i,2j,2k} \approx \frac{d_{2i,2j,2k+1}-d_{2i,2j,2k-1}}{\Delta z_{2i,2j}}$$

$$- \frac{\psi\Delta t}{(\Delta z_{2i,2j})^2}(P^{*n+1}_{2i,2j,2k+2} - 2P^{*n+1}_{2i,2j,2k} + P^{*n+1}_{2i,2j,2k-2}) \tag{27}$$

Also, derivative of the orthogonal to the plane velocity, i.e. v is in the form as given below:

$$\left(\frac{\partial v}{\partial y}\right)^{n+\alpha}_{2i,2j,2k} \approx \sum_{j1=1}^{2}\sum_{j2=1}^{3} r(yz)^{2i,2j,2k}_{j1,j2} v^{n+\alpha}_{2i,m_{2j}(j1),n_{2k}(j2)} \tag{28}$$

Substituting Equations (26)–(28) into continuity equation (14), the velocities are eliminated giving an equation in term of the pressures as

$$\psi\Delta t \sum_{j1=1}^{2}\sum_{j2=1}^{3} r(xz)^{2i,2j,2k}_{j1,j2} \left(\sum_{j3=1}^{2}\sum_{j4=1}^{3} r(xz)^{m_{2i}(j1),2j,n_{2k}(j2)}_{j3,j4} P^{*n+1}_{m_{m_{2i}(j1)}(j3),2j,n_{n_{2k}(j2)}(j4)}\right)$$

$$+\frac{\psi\Delta t}{(\Delta z_{2i,2j})^2}(P^{*n+1}_{2i,2j,2k+2} - 2P^{*n+1}_{2i,2j,2k} + P^{*n+1}_{2i,2j,2k-2})$$

$$= \sum_{j1=1}^{2}\sum_{j2=1}^{3} r(xz)^{2i,2j,2k}_{j1,j2} d_{m_{2i}(j1),2j,n_{2k}(j2)} + \sum_{j1=1}^{2}\sum_{j2=1}^{3} r(yz)^{2i,2j,2k}_{j1,j2} v^{n+\alpha}_{2i,m_{2j}(j1),n_{2k}(j2)}$$

$$+\frac{d_{2i,2j,2k+1}-d_{2i,2j,2k-1}}{\Delta z_{2i,2j}} \tag{29}$$

DOI: 10.1002/fld

New top-layer treatment: The following equation can be written for the mass conservation at column $(2i, 2j)$:

$$\frac{\xi^{n+1}_{2i,2j} - \xi^{n}_{2i,2j}}{\Delta t} + \frac{\theta}{\Delta x_{2i,2j}} \sum_{k=1}^{nk} (\Delta z_{2i+1,2j} u^{n+1}_{2i+1,2j,2k} - \Delta z_{2i-1,2j} u^{n+1}_{2i-1,2j,2k})$$
$$+ \frac{(1-\theta)}{\Delta x_{2i,2j}} \sum_{k=1}^{nk} (\Delta z_{2i+1,2j} u^{n}_{2i+1,2j,2k} - \Delta z_{2i-1,2j} u^{n}_{2i-1,2j,2k})$$
$$+ \frac{\theta}{\Delta y_{2i,2j}} \sum_{k=1}^{nk} (\Delta z_{2i,2j+1} v^{n+\alpha}_{2i,2j+1,2k} - \Delta z_{2i,2j-1} v^{n+\alpha}_{2i,2j-1,2k})$$
$$+ \frac{(1-\theta)}{\Delta y_{2i,2j}} \sum_{k=1}^{nk} (\Delta z_{2i,2j+1} v^{n}_{2i,2j+1,2k} - \Delta z_{2i,2j-1} v^{n}_{2i,2j-1,2k}) = 0 \tag{30}$$

where nk is the number of layers and the implicit weighting factor θ, is taken as 0.5. Vertical momentum equation (17) in column $(2i, 2j)$ from the centre of top layer, to the free surface is approximated by

$$\frac{w^{n+1}_{2i,2j,T} - w^{**}_{2i,2j,T}}{\Delta t} + \psi \left(\frac{P^{*n+1}_{2i,2j,S} - P^{*n+1}_{2i,2j,2nk}}{\Delta z_{2i,2j}/2} \right) + (1-\psi) \left(\frac{P^{*n}_{2i,2j,S} - P^{*n}_{2i,2j,2nk}}{\Delta z_{2i,2j,}/2} \right) = 0 \tag{31}$$

where T is the index for the vertical position of the top layer. $P^{*n+1}_{2i,2j} = g\xi^{n+1}_{2i,2j}$ and $P^{*n}_{2i,2j,S} = g\xi^{n}_{2i,2j}$ are pressure at surface water level. $w^{n+1}_{2i,2j,.T}$ is the vertical velocity at top layer located at a distance of $0.25\Delta z_{2i,2j}$ from the surface. Yuan and Wu [8] suggested a simple averaging $w^{n+1}_{2i,2j,T}=(w^{n+1}_{2i,2j,2nk-1}+w^{n+1}_{2i,2j,2nk+1})/2$. However, their model yields acceptable results only by employing large number of vertical layers (for example, 20 in the case of linear sinusoidal short wave simulation). A linear approximation $w^{n+1}_{2i,2j.T} = 0.25w^{n+1}_{2i,2j,2nk-1} + 0.75w^{n+1}_{2i,2j,2nk+1}$ seems to be a better choice considering the location of $w^{n+1}_{2i,2j,.T}$. Yet $w^{n+1}_{2i,2j,.T}$ can be approximated with higher-order accuracy, for instance, with a third-order approximation as follows:

$$w^{n+1}_{2i,2j,T} = f_1 w^{n+1}_{2i,2j,2nk+1} + f_2 w^{n+1}_{2i,2j,2nk-1} + f_3 w^{n+1}_{2i,2j,2nk-3} + f_4 w^{n+1}_{2i,2j,2nk-5} \tag{32}$$

where $f_1 = \frac{77}{128}$, $f_2 = \frac{77}{128}$, $f_3 = -\frac{33}{128}$ and $f_4 = \frac{7}{128}$.

The improvement caused by applying linear approximation is also confirmed by Yuan and Wu [16].

Substituting $w^{n+1}_{2i,2j,T}$ from one of the approximation mentioned above (for example, linear approximation); $\xi^{n+1}_{2i,2j}$ from Equation (30); $u^{n+1}_{2i-1,2j,2k}$ from Equation (20); $w^{n+1}_{2i,2k-1}$ from Equation (22); and $w^{n+1}_{2i,2nk+1}$ from continuity equation (14), into Equation (31), the velocities are eliminated and the pressure equation of the upper layer is obtained as follows:

$$0.75\frac{\psi\Delta t\Delta z_{2i,2j}}{\Delta t} \sum_{j1=1}^{2} \sum_{j2=1}^{3} r(xz)^{2i,2j,2nk}_{j1,j2} \sum_{j3=1}^{2} \sum_{j4=1}^{3} r(xz)^{m_{2i}(j1),2j,n_{2nk}(j2)}_{j3,j4}$$

DOI: 10.1002/fld

$$\times P^{*n+1}_{m_{m_{2i}(j1)}(j3),2j,n_{n_{2nk}(j2)}(j4)} + \frac{2g\theta\Delta z_{2i+1,2j}(\psi\Delta t)^2}{\Delta z_{2i,2j}\Delta x_{2i,2j}} \sum_{k=1}^{nk}\sum_{j1=1}^{2}\sum_{j2=1}^{3} r(xz)^{2i+1,2j,2k}_{j1,j2}$$

$$\times P^{*n+1}_{m_{2i+1}(j1),2j,n_{2k}(j2)} - \frac{2g\theta\Delta z_{2i-1,2j}(\psi\Delta t)^2}{\Delta z_{2i,2j}\Delta x_{2i,2j}} \sum_{k=1}^{nk}\sum_{j1=1}^{2}\sum_{j2=1}^{3} r(xz)^{2i-1,2j,2k}_{j1,j2}$$

$$\times P^{*n+1}_{m_{2i-1}(j1),2j,n_{2k}(j2)} - \frac{3\psi}{\Delta z_{2i,2j}} P^{*n+1}_{2i,2j,2nk} + \frac{\psi}{\Delta z_{2i,2j}} P^{*n+1}_{2i,2j,2nk-2}$$

$$= + \frac{2\psi g\Delta t(1-\theta)}{\Delta z_{2i,2j}\Delta x_{2i,2j}} \sum_{k=1}^{nk} (\Delta z_{2i+1,2j} u^n_{2i+1,2j,2k} - \Delta z_{2i-1,2j} u^n_{2i-1,2j,2k})$$

$$+ 0.75\frac{\Delta z_{2i,2j}}{\Delta t}\left(\sum_{j1=1}^{2}\sum_{j2=1}^{3} r(yz)^{2i,2j,2nk}_{j1,j2} v^{n+\alpha}_{2i,m_{2j}(j1),n_{2nk}(j2)}\right)$$

$$+ \frac{2\psi g\Delta t}{\Delta z_{2i,2j}\Delta y_{2i,2j}} \sum_{k=1}^{nk} (\theta\Delta z_{2i,2j+1} v^{n+\alpha}_{2i,2j+1,2k} - \theta\Delta z_{2i,2j-1} v^{n+\alpha}_{2i,2j-1,2k}$$

$$+ (1-\theta)\Delta z_{2i,2j+1} v^{n}_{2i,2j+1,2k} - (1-\theta)\Delta z_{2i,2j-1} v^{n}_{2i,2j-1,2k})$$

$$+ \frac{2\psi\theta g\Delta t}{\Delta z_{2i,2j}\Delta x_{2i,2j}}\left(\sum_{k=1}^{nk}\Delta z_{2i+1,2j} d_{2i+1,2j,2k} - \sum_{k=1}^{nk}\Delta z_{2i-1,2j} d_{2i-1,2j,2k}\right)$$

$$+ 0.75\frac{\Delta z_{2i,2j}}{\Delta t}\sum_{j1=1}^{2}\sum_{j2=1}^{3} r(xz)^{2i,2j,2nk}_{j1,j2} d^{n+1}_{m_{2i}(j1),2j,n_{2nk}(j2)} - \frac{d_{2i,2j,2nk-1}}{\Delta t}$$

$$- \frac{2g}{\Delta z_{2i,2j}}\xi^n_{2i,2j} + \frac{2(1-\psi)}{\Delta z_{2i,2j}} P^{*n}_{2i,2j,2nk} + 0.25\frac{w^{**}_{2i,2j,2nk-1}}{\Delta t} + 0.75\frac{w^{**}_{2i,2j,2nk+1}}{\Delta t} \tag{33}$$

Pressure equation (33) for the top layer together with the pressure equations of the lower layers (29) form a tri-diagonal block matrix system which can be solved by a direct matrix solver. The details of this solution method have been described in [10]. After the solution of unknown pressure horizontal flow velocity u, vertical velocity w and free-surface elevation are updated by back substitution in Equations (20), (22) and (30), respectively.

Solution of equations in y–z planes: The solution in these planes is similar to x–z plane described above.

4. MODEL VALIDATIONS

4.1. Linear 3D standing short wave in deep water

A linear 3D standing short wave in deep water assuming an inviscid flow is the first test representing the effects of hydrodynamic pressure distribution on model results. The uninodal sinusoidal wave oscillates in a $10 \times 10 \times 10\,\mathrm{m}^3$ basin with amplitude of $A = 0.1$. Figure 2 shows initial free surface. The analytical solution for linear wave period and celerity is $T = 3.01$ s and $c = 6.64$ m/s,

DOI: 10.1002/fld

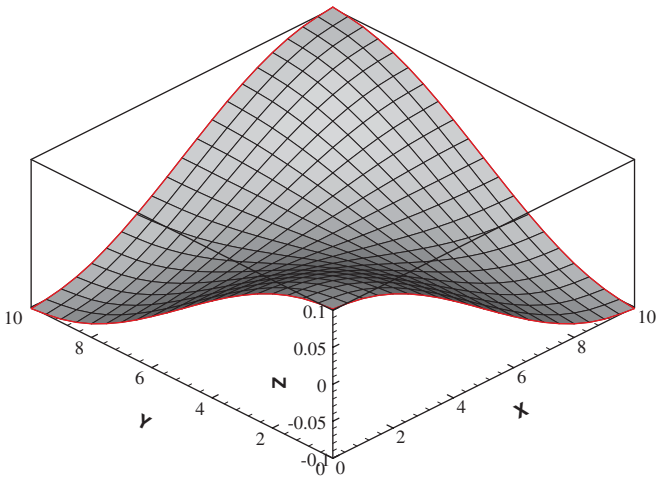

Figure 2. Initial free surface for 3D standing wave oscillating in a closed reservoir.

respectively. The linear wave theory is valid in this case. Details of analytical solutions of the linear standing wave can be found in [9, 19]. The numerical parameters used in this test case are: $\Delta x = 0.5$ m, $\Delta y = 0.5$ m, $\Delta t = 0.05$ s. As mentioned before in 'top layer treatment' three approximations can be used for vertical velocity in top layer: simple averaging approximation, linear approximation and third-order approximation. In Figure 3, different results obtained by applying these three approximations at the top layer are presented. Weak approximations cause noticeable phase error especially with small number of vertical layers. On the contrary, third-order approximation yields a more accurate simulation of wave celerity, using only four vertical layers.

An iteration procedure has been used to assure the convergence of 3D solution. The convergence criterion for the error in calculated velocities is chosen to be $\varepsilon = 0.0008|\text{velocity}_{\max}|$, where $\text{velocity}_{\max}$ is the maximum expected velocity. Table I shows average CPU time and the number of iterations for different number of layers.

Furthermore a grid convergence index (GCI) proposed by Roache [20] is applied to check grid convergence and to confirm accuracy of a set-up with 20×20 horizontal grids, four vertical layers, and a time step of 0.05 s. Computed free-surface elevation at $(x, y) = (0.25\,\text{m}, 0.25\,\text{m})$ and $t = 5\text{T}$ has been chosen for comparing errors between coarse and fine grids. For the fine grid, GCI is defined as follows [20]:

$$\text{GCI}_{\text{fine}} = \frac{3|\text{error}|}{r^p - 1}$$
$$\text{error} = (f_{\text{coarse}} - f_{\text{fine}})/f_{\text{fine}} \tag{34}$$

where r is the grid refinement ratio, p is the order of convergence and f is an evaluated quantity. In this example, p is set to be unity and maximum of calculated free surface is selected as evaluated quantity. Information on grids and calculated GCI_{fine} has been summarized in Table II. The results confirm sufficiency of using four vertical layers and 20×20 horizontal grid for computing free-surface elevation.

DOI: 10.1002/fld

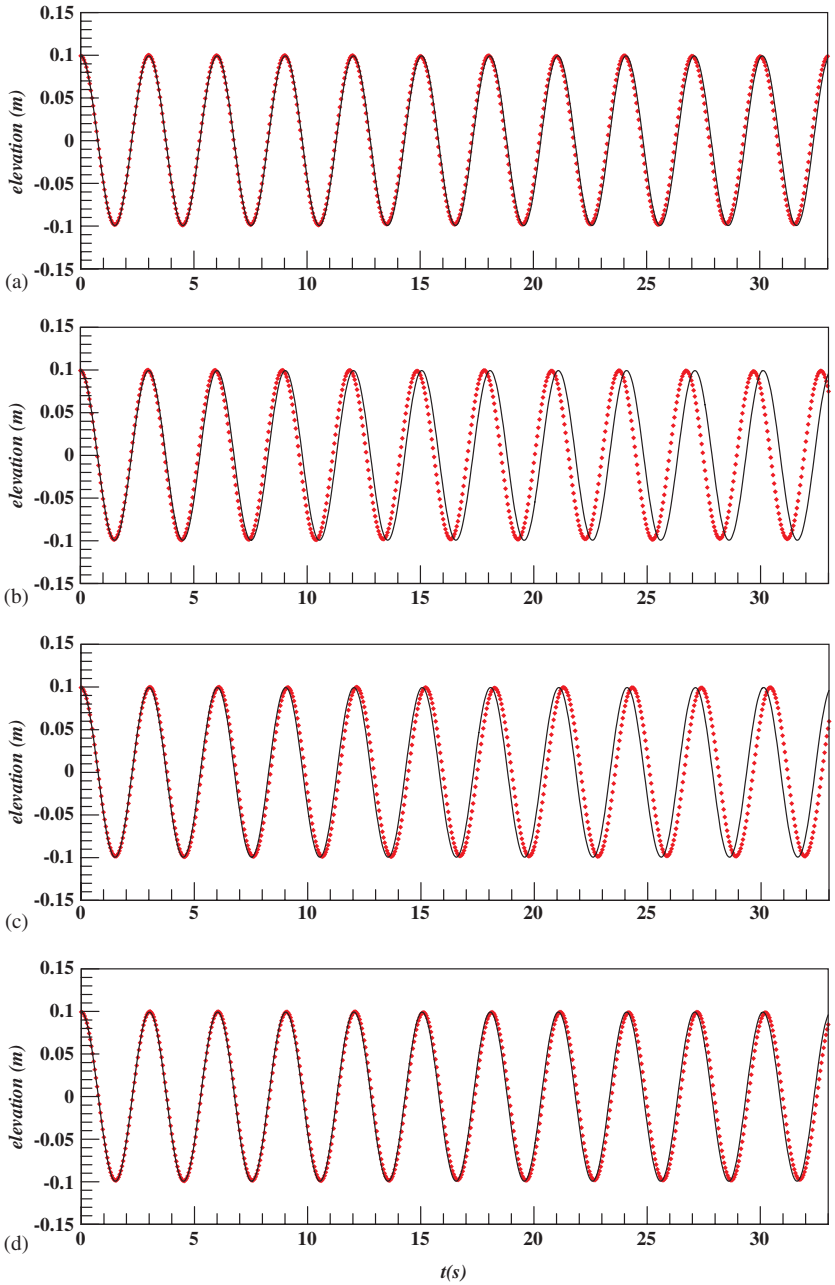

Figure 3. Comparisons of free-surface elevation for 3D linear standing wave test at $x = 0.25$ m and $y = 0.25$ m, between analytical solutions (solid lines) and numerical results (dots) for different models: (a) simple averaging top-layer approximation with 15 vertical layers; (b) simple averaging top-layer approximation with four vertical layers; (c) linear top-layer approximation with four vertical layers; and (d) third-order top-layer approximation with four vertical layers.

DOI: 10.1002/fld

Table I. Average number of iterations and CPU time for each time step using an Intel Pentium 4—3:00 GHz computer.

Number of vertical layers	Number of iterations	Average CPU time (s)
4	4.27	0.19
8	4.25	0.50
15	4.22	1.47
30	4.20	6.13

Table II. Summary of grid convergence test.

Coarse grid	Δt_{coarse}	Fine grid	Δt_{fine}	grid refinement ratio (r)	GCI_{fine} (%)
$20 \times 20 \times 4$	0.05	$40 \times 40 \times 8$	0.025	2	0.98
$20 \times 20 \times 4$	0.05	$20 \times 20 \times 16$	0.05	4	0.82

4.2. Linear progressive wave

A 2D linear progressive wave with a height of 1 m propagates over a constant depth of 100 m. These conditions satisfy the range of validity of linear wave theory [19]. A sinusoidal velocity distribution based on linear theory is imposed at the left boundary. A combination of a sponge layer and a radiation boundary condition is applied at the outflow (right) boundary. To generate various kh values, where k represents the wave number, two wave periods i.e. $T = 10$ s (deep water with $kh = 4.03$) and $T = 15$ s (intermediate water depth with $kh = 1.87$) are tested. The numerical parameters used in this test case are: $\Delta x = L/20$, $\Delta t = T/60$. The accuracy of the model is measured by a normalized percentage error (e), defined by $e = |c_{\text{analytical}} - c_{\text{model}}|/c_{\text{analytical}} * 100\%$, where c_{model} and $c_{\text{analytical}}$ are wave celerity from the model calculation and analytical solutions, respectively. Three approximations can be used for vertical velocity in top layer; simple averaging, linear approximation and third-order approximation. In Figure 4, the results obtained by applying these three approximations at top layer are presented. Furthermore, normalized percentage errors for different number of layers and wave numbers are compared in Table III. Simple approximation cause noticeable phase error especially with small number of vertical layers. On the contrary, third-order approximation yields a more accurate simulation of wave celerity. With moving from intermediate depth to deep water the errors are increased. For instance for $kh = 4.03$, linear and third-order approximations reach good results using 10 and 5 layers, respectively.

4.3. Solitary wave propagation in a variable water depth

Solitary wave propagation over uneven water depths is an appropriate test to evaluate the capability of model in nonlinear wave simulation. Flow is assumed to be inviscid. Numerical results are compared with a set of analytical/theoretical solution and experimental data originally reported in Madsen and Mei [21]. Figure 5 shows the experimental set-up. At the deep section of the flume, the wave amplitude to water depth ratio is $A_0/h_0 = 0.12$. Six hundred grid points is chosen in longitudinal direction and numerical time step is 0.005 s. The initial position of wave crest is located at $x = -0.8\,m$. A known velocity distribution obtained from analytical solution [22] is considered at the left boundary and a radiation boundary is applied to the right. Water surface profiles at four locations are compared between numerical results with 2 and 10 vertical layers,

DOI: 10.1002/fld

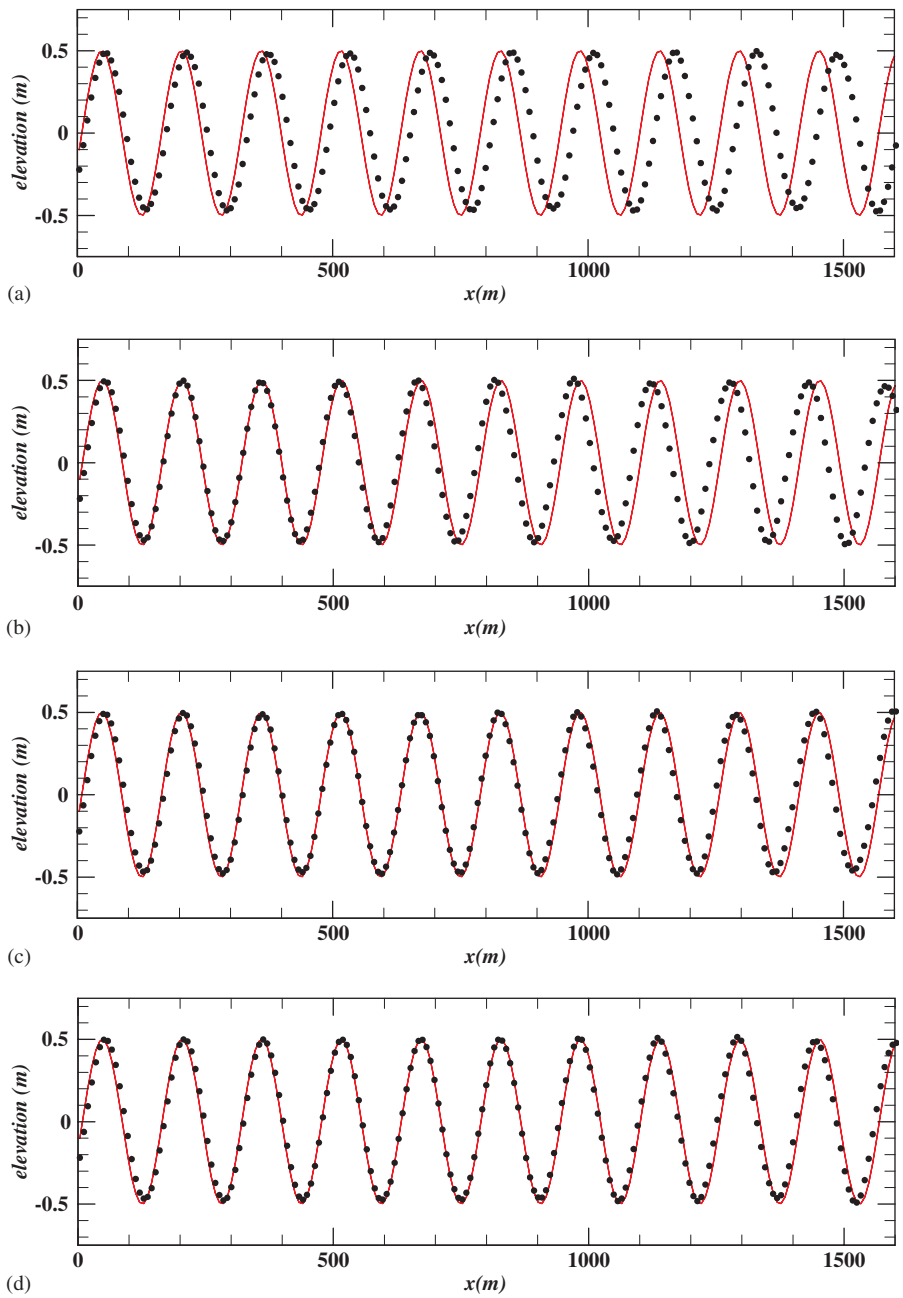

Figure 4. Comparisons of free-surface elevation for linear progressive wave test ($T = 10\,\mathrm{s}, kh = 4.03$), between analytical solutions (solid lines) and numerical results (dots) for different models: (a) simple averaging top-layer approximation with five vertical layers; (b) linear top-layer approximation with five vertical layers; (c) third-order top-layer approximation with five vertical layers; and (d) linear top-layer approximation with 10 vertical layers.

DOI: 10.1002/fld

Table III. Comparison of normalized percentage error for different number of layers, *kh* and approximation methods used for vertical velocity at the top layer.

Number of layers	*kh*	Approximation method	*e*
3	1.87	Simple averaging	0.89
3	1.87	Linear	0.85
3	1.87	Third order	0.82
7	1.87	Simple averaging	0.24
3	4.03	Simple averaging	3.33
3	4.03	Linear	4.88
3	4.03	Third order	2.34
5	4.03	Simple averaging	1.93
5	4.03	Linear	1.75
5	4.03	Third order	0.66
10	4.03	Linear	0.79
15	4.03	Simple averaging	0.61

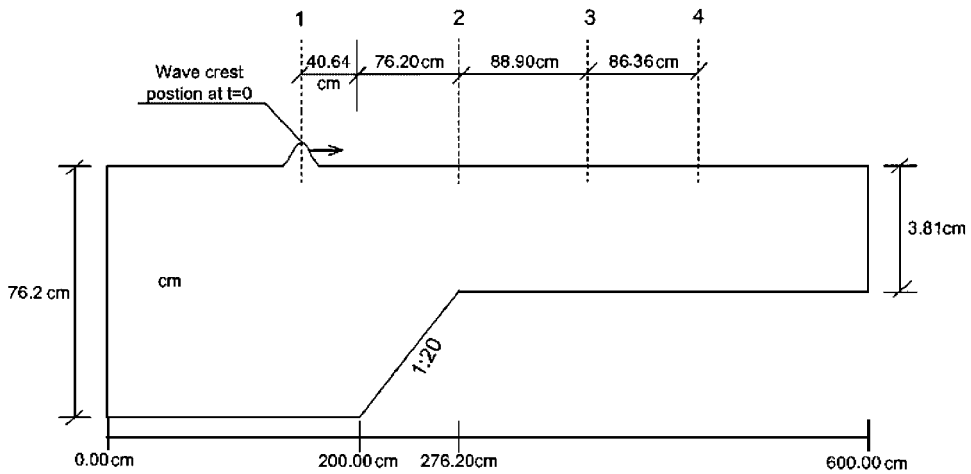

Figure 5. Flume geometry for solitary wave propagation over variable water depth.

theoretical predictions and estimated experimental data for non-viscous damping are presented in Figure 6. The numerical results exhibit the fission phenomenon [23] quite well. In Figure 6, only the water surface profiles are compared. At position 4, the numerical results with two vertical layers show a relative height of 149% for the larger wave and 52% for the smaller one, representing the ability of modelling with very few vertical layers.

4.4. Wave propagation over a submerged elliptic shoal

To validate the 3D model in simulating wave phenomena such as shoaling, refraction and diffraction and also dynamic pressure and nonlinear behaviour, 3D wave transformation over a submerged elliptic shoal is tested and compared with Vincent and Briggs [24] experimental data. This is a classical example in which a non-breaking monochromatic wave transforms over 3D uneven bottom, and has been studied with various depth-integrated models [16]. Figure 7 depicts the

DOI: 10.1002/fld

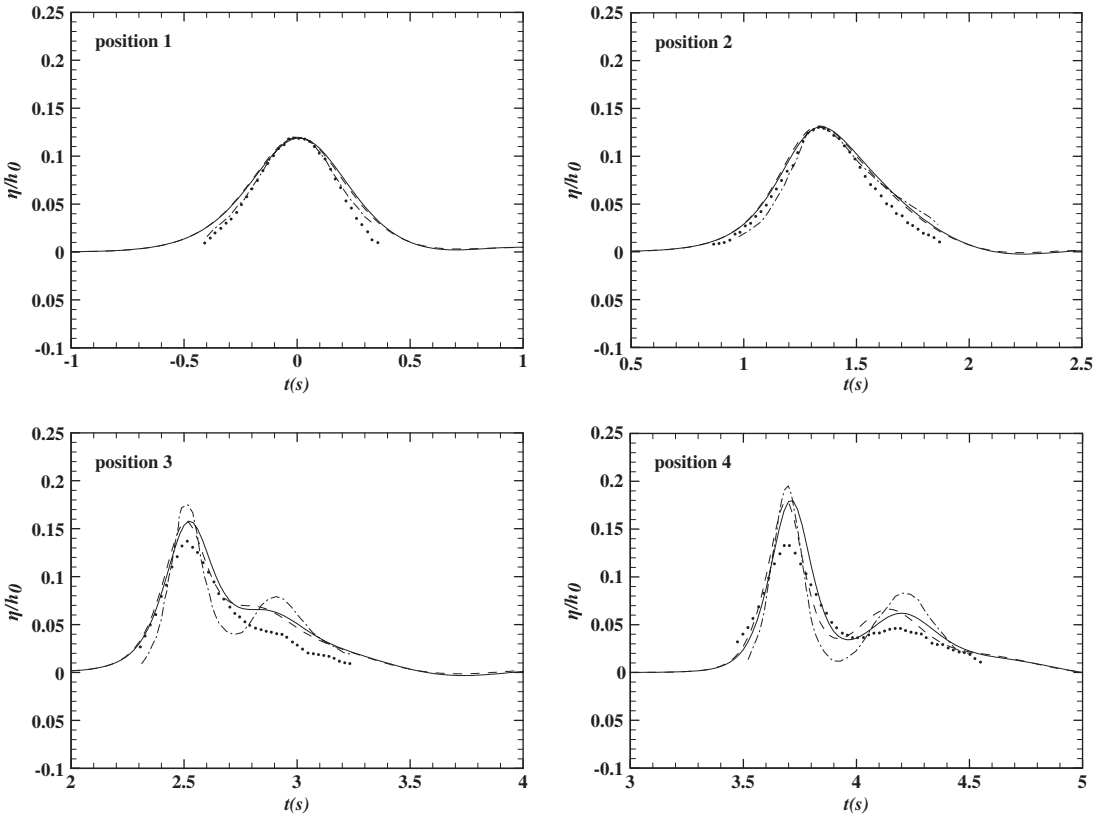

Figure 6. Comparison of the free-surface elevation for solitary wave propagation over variable water depth at locations 1, 2, 3 and 4 between numerical results using two layers (solid line), numerical results using 10 layers (dashed line), theoretical predictions (dash-dot line) and estimated experimental data for non-viscous damping (dots).

experimental set-up, including a shoal with an elliptic boundary described as

$$\left(\frac{x}{3.05}\right)^2 + \left(\frac{y}{3.96}\right)^2 = 1 \tag{35}$$

The elevation inside the elliptic shoal is obtained by following relationship:

$$d = 0.9144 - 0.762\sqrt{1 - \left(\frac{x}{3.81}\right)^2 - \left(\frac{y}{4.95}\right)^2} \tag{36}$$

Outside the shoal, water depth is equal to 0.457 m. At the inflow boundary, an incoming wave with a height and period equal to $H_0 = 2.54$ cm and $T_0 = 1.3$ s, respectively is enforced based on linear wave theory. At the outflow, a sponge layer is used to absorb outgoing waves. In lateral boundaries, no-slip condition with impermeable wall is applied. The computational domain is $25 \times 25\,\mathrm{m}^2$, discretized by a set of 500×250 horizontally uniform grids in x and y directions, respectively. Having shown the accuracy and efficiency of the model, only two layers are deployed in vertical direction. The time step is taken as 0.02 s and the total simulation time is

DOI: 10.1002/fld

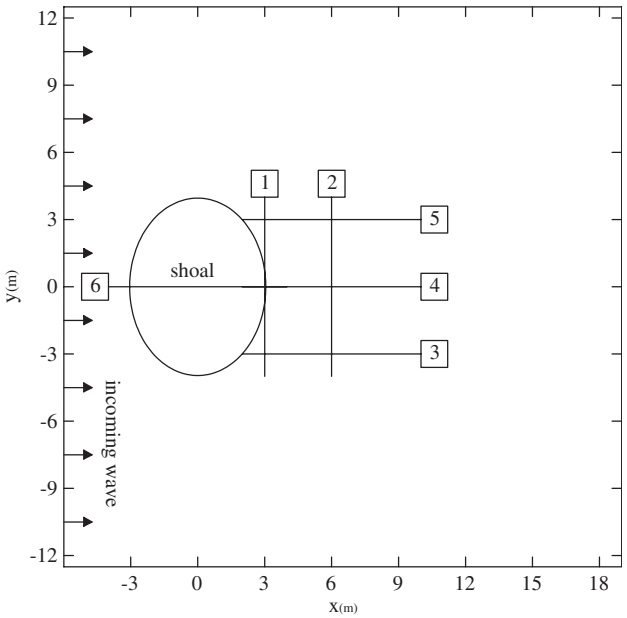

Figure 7. Experimental set-up and measurement sections according to Vincent and Briggs [24].

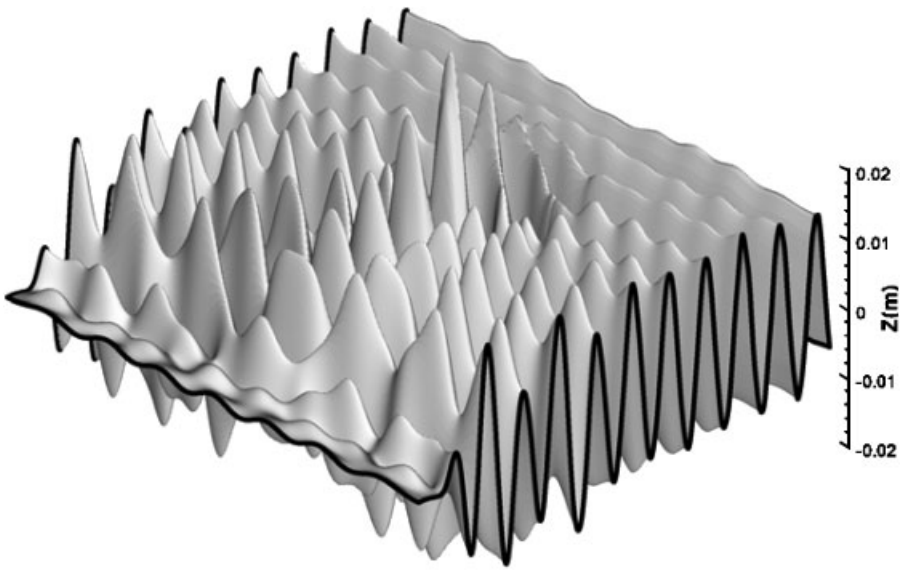

Figure 8. 3D sketch of stationary wave field at the end of simulation time.

32 s reaching a stationary wave field shown in Figure 8. The final wave height was obtained by averaging on the last four wave periods. An average of about three iterations is required for each time step.

DOI: 10.1002/fld

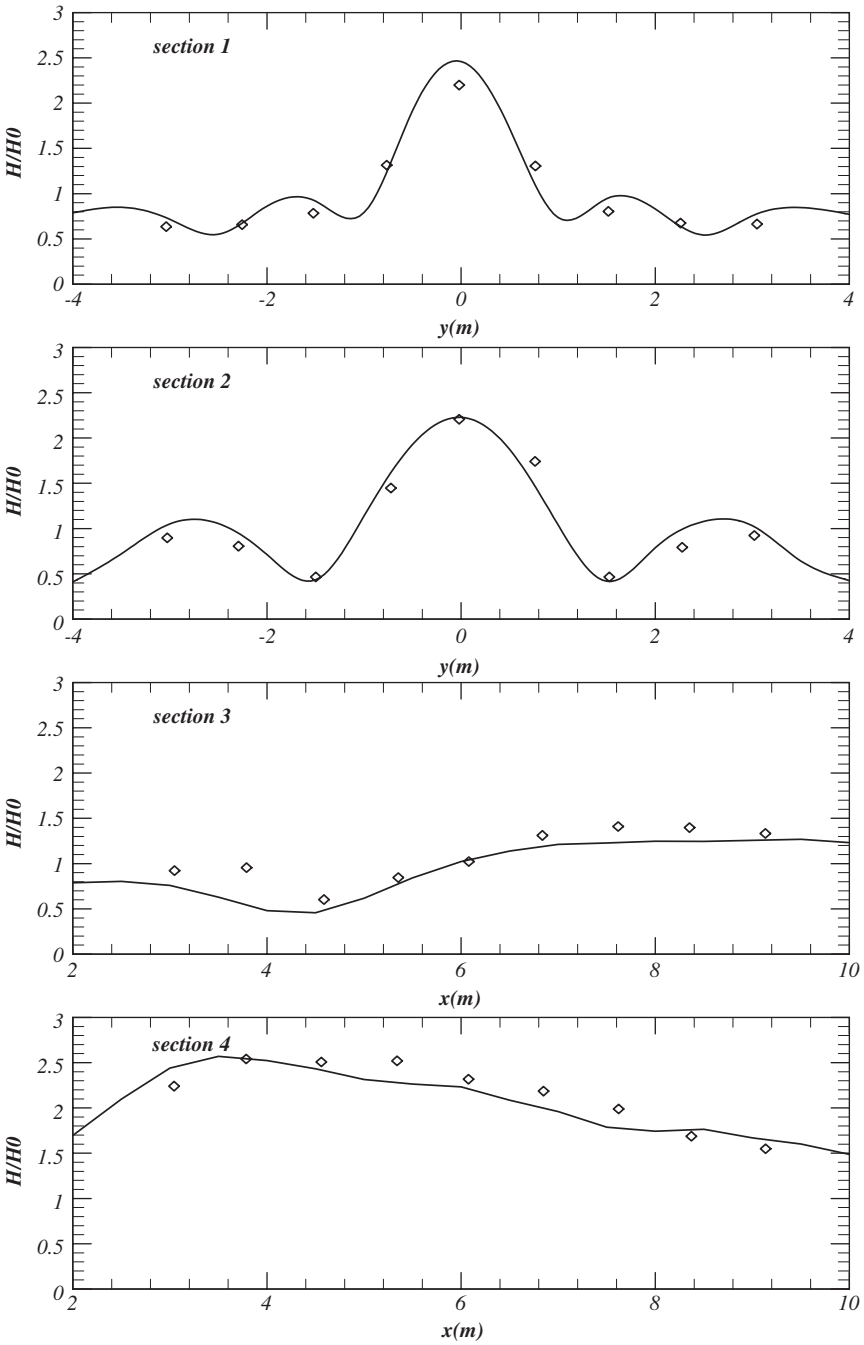

Figure 9. Comparison of normalized wave heights between numerical results (solid line) and experimental data (diamonds) at six sections.

DOI: 10.1002/fld

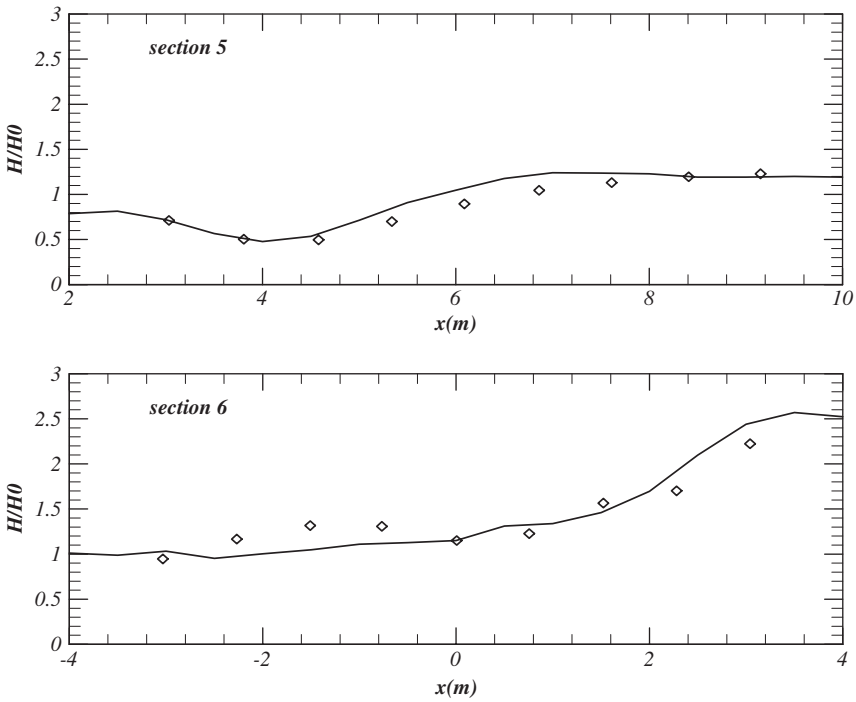

Figure 9. *Continued.*

The numerical predicted normalized wave heights and experimental corresponding data have been compared in Figure 9 at six cross-sections. In Section 6, where waves propagated over the elliptic shoal, the model acceptably predicts shoaling effects. In Sections 1 and 2, the focusing effect has been satisfactorily simulated by the model where the maximum normalized wave height is about 2.45 and 2.25, respectively. In Sections 3, 4, and 5 along the x direction, the model results are generally close to the experimental data. Maximum wave height appears around $x = 3.5$ m along Section 4 with an amplification factor about 2.55. After the peak location, lateral distribution of wave energy causes the wave height to reduce. Satisfactory results obtained by the model with only two vertical layers not only reduce the computational cost severely, but also demonstrate its ability in simulating refraction and diffraction caused by an irregular submerged shoal.

5. CONCLUSIONS

As an extension to previous 2D paper [10], an efficient 3D fully dynamic model based on finite volume method is developed to simulate free-surface flows. Employment of vertical boundary fitted coordinate ensures an accurate representation of flow at bed and free surface. The new treatment of non-hydrostatic pressure at the top layer makes the model to simulate complicated free-surface flow problems with a very small number of vertical layers accurately and free of any hydrostatic pressure assumption.

DOI: 10.1002/fld

'Projection method' has been chosen as numerical technique in which the momentum equations are solved without the pressure terms in the first step. This step is called the 'advection–diffusion' step. In the second step, continuity equation, together with momentum equations without advection and diffusion terms are solved. In this step, the whole 3D problem is decomposed into a series of 2DV sub-domains as proposed by [9] by treating orthogonal to the plane derivatives as temporary known terms. Each 2DV sub-systems can be solved by a direct matrix solver. Finally, an iteration procedure is used to assure convergence. The matrix system is a quarter in size as compared to methods which solve equations in one step simultaneously [17]. In addition, different numerical schemes for each step can be used within this algorithm. Since the domain decomposition is identical in two horizontal directions and each 2DV problem is independent, the algorithm is potentially suitable for parallel computations.

To validate the model, four tests including complicated free surface were performed with only 2–5 vertical layers. In modelling 3D standing linear short wave and linear progressive wave, it was shown by deploying new top-layer treatment, the number of vertical layers can be reduced noticeably. This treatment reduces the computational cost severely. The model predicts solitary wave propagation over an uneven bottom satisfactorily. The results predicted by 2 and 10 vertical layers are very close to each other. At last in the test of 3D wave propagation over a submerged elliptic shoal close agreement between numerical results and experimental data assures the capability of model for the simulation of 3D wave propagation including dispersion, shoaling, refraction and diffraction phenomena.

ACKNOWLEDGEMENTS

The work reported herein was supported by a grant from the Water Resources Management Co. under the Project Number RIV1-83084 and the Faculty of Civil Engineering, School of Engineering, University of Tehran. Their support is gratefully acknowledged.

REFERENCES

1. Chorin AJ. Numerical solution of the Navier–Stokes equations. *Mathematics of Computation* 1968; **22**:745–762.
2. Li B, Fleming C. Three-dimensional model of Navier–Stokes equations for water waves. *Journal of Waterway*, Port, Coastal, and Ocean Engineering (ASCE) 2001; **January**/**February**:16–25.
3. Lin P, Li C. A σ-coordinate three-dimensional numerical model for surface wave propagation. *International Journal for Numerical Methods in Fluids* 2002; **38**:1045–1068.
4. Casulli V. A semi-implicit finite difference method for non-hydrostatic, free-surface flows. *International Journal for Numerical Methods in Fluids* 1999; **30**:425–440.
5. Kocyigit MB, Falconer RA, Lin B. Three-dimensional numerical modelling of free-surface flows with nonhydrostatic pressure. *International Journal for Numerical Methods in Fluids* 2002; **40**:1145–1162.
6. Chen X. A fully hydrodynamic model for three-dimensional, free-surface flows. *International Journal for Numerical Methods in Fluids* 2003; **42**(9):929–952.
7. Namin M, Lin B, Falconer R. An implicit numerical algorithm for solving non-hydrostatic free-surface flow problems. *International Journal for Numerical Methods in Fluids* 2001; **35**:341–356.
8. Yuan HL, Wu CH. A two-dimensional vertical non-hydrostatic σ model with an implicit method for free-surface flows. *International Journal for Numerical Methods in Fluids* 2004; **44**:811–835.
9. Yuan HL, Wu CH. An implicit three-dimensional fully non-hydrostatic model for free-surface flows. *International Journal for Numerical Methods in Fluids* 2004; **46**:709–733.
10. Ahmadi A, Badiei P, Namin M. An implicit two-dimensional non-hydrostatic model for free-surface flows. *International Journal for Numerical Methods in Fluids* 2007; **54**(9):1055–1074.
11. Park JC, Kim MH, Miyata H. Fully non-linear free-surface simulations by a 3D viscous numerical wave tank. *International Journal for Numerical Methods in Fluids* 1999; **29**(6):685–703.

DOI: 10.1002/fld

12. Hur DS, Mizutani N. Numerical estimation of the wave forces acting on a three-dimensional body on submerged breakwater. *Coastal Engineering* 2003; **47**:329–345.
13. Hodges BR, Street RL. On simulation of turbulent nonlinear free-surface flows. *Journal of Computational Physics* 1999; **151**(2):425–457.
14. Yue WS, Lin CL, Patel VC. Numerical simulation of unsteady multidimensional free-surface motions by level set method. *International Journal for Numerical Methods in Fluids* 2004; **42**:853–884.
15. Stelling G, Zijlema M. An accurate and efficient finite-difference algorithm for non-hydrostatic free-surface flow with application to wave propagation. *International Journal for Numerical Methods in Fluids* 2003; **43**:1–23.
16. Yuan HL, Wu CH. Fully non-hydrostatic modelling of surface waves. *Journal of Engineering Mechanics* 2006; **132**(4):447–456.
17. Choi DU, Wu CH. A new efficient 3D non-hydrostatic free-surface flow model for simulating water wave motions. *Ocean Engineering* 2006; **33**:587–609.
18. Lee JW, Teubner MD, Nixon JB, Gill PM. A 3-D non-hydrostatic pressure model for small amplitude free-surface flows. *International Journal for Numerical Methods in Fluids* 2006; **50**:649–672.
19. Dean RG, Dalrymple RA. *Water Wave Mechanics for Engineers and Scientists*. World Scientific: Singapore, 2000.
20. Roache PJ. Perspective: a method for uniform reporting of grid refinement studies. *Journal of Fluids Engineering* 1994; **116**:405–413.
21. Madsen OS, Mei CC. The transformation of a solitary wave over an uneven bottom. *Journal of Fluid Mechanics* 1969; **39**(4):781–791.
22. Sorensen RM. *Basic Coastal Engineering*. Kluwer: New York, 1997.
23. Mei CC. *The Applied Dynamics of Ocean Surface Waves*. Wiley: New York, 1983.
24. Vincent CL, Briggs MJ. Refraction–diffraction of irregular waves over a mound. *Journal of Waterway, Port, Coastal, and Ocean Engineering* (ASCE) 1989; **2**:269–284.

DOI: 10.1002/fld